UC Berkeley

UC Berkeley Previously Published Works

Title

Nanometer-Resolved Spectroscopic Study Reveals the Conversion Mechanism of CaO·Al2O3·10H2O to 2CaO·Al2O3·8H2O and 3CaO·Al2O3·6H2O at an Elevated Temperature

Authors

Geng, Guoqing

Li, Jiaqi

Yu, Young-Sang

et al.

Nanometer-Resolved Spectroscopic Study Reveals the Conversion Mechanism of CaO·Al$_2$O$_3$·10H$_2$O to 2CaO·Al$_2$O$_3$·8H$_2$O and 3CaO·Al$_2$O$_3$·6H$_2$O at an Elevated Temperature

Guoqing Geng,[†] Jiaqi Li,[†] Young-Sang Yu,[‡] David A. Shapiro,[‡] David A. L. Kilcoyne,[‡] and Paulo J. M. Monteiro*,[†,§]

[†]Department of Civil and Environmental Engineering, University of California, Berkeley, California 94720, United States

[‡]Advanced Light Source and [§]Material Science Division, Lawrence Berkeley National Laboratory, Berkeley, California 94720, United States

Ⓢ Supporting Information

ABSTRACT: The main binding phases of calcium aluminate cement (CAC) concrete, CaO·Al$_2$O$_3$·10H$_2$O (CAH$_{10}$) and 2CaO·Al$_2$O$_3$·8H$_2$O (C$_2$AH$_8$), slowly convert to 3CaO·Al$_2$O$_3$·6H$_2$O (C$_3$AH$_6$) and Al(OH)$_3$ (AH$_3$). This reaction significantly speeds up at a temperature higher than ~30 °C, and over time leads to significant strength loss in CAC concrete. Because of the lack of direct evidence that simultaneously probes morphological and chemical/crystallographic information, intense debate remains whether the conversion is generated by a solid-state or through-solution reaction. The conversion of CAH$_{10}$ at an elevated temperature is studied herein using synchrotron-radiation-based X-ray spectromicroscopy capable of acquiring near edge X-ray absorption fine structure data and ptychographic images with a resolution of ~15 nm. We show that, when stored at 60 °C, CAH$_{10}$ first converts to C$_2$AH$_8$ by solid-state decomposition, followed by the through-solution formation of C$_3$AH$_6$. The C$_3$AH$_6$ crystallizes from both the relics of dissolved C$_2$AH$_8$ and from the surface of existing C$_3$AH$_6$ crystals. The solid-state decomposition of CAH$_{10}$ occurs in multiple sites inside the CAH$_{10}$ crystals; the spatial range of each decomposition site spans a few tens of nanometers, which overcomes the kinetics barrier of ion transportation in the solid-state. Our work provides the first nanoscale crystal−chemical evidence to explain the microstructure evolution of converted CAC concrete.
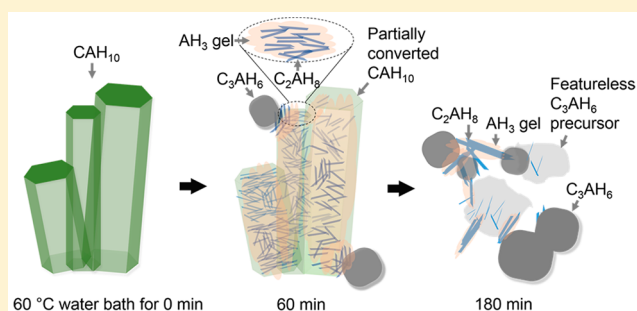
INTRODUCTION

The unique hydration behavior of calcium aluminate cement (CAC), such as high reactivity (even at low-curing temperatures), leads to its broad application in emergency repair, fast-track construction in cold weather, and infrastructures exposed to sulfate attack; it is also widely used to make refractory linings for high-temperature furnaces.[1,2] Calcium aluminate cement contains CA (monocalcium aluminate) as the main cementing compound, with C$_{12}$A$_7$, C$_2$, and CA$_6$ as the minor phases, where C=CaO, A=Al$_2$O$_3$, and H=H$_2$O in the cement chemistry notation.[3,4] The rapid hydration of CA produces CAH$_{10}$ and C$_2$AH$_8$ + AH$_3$ at ambient temperature and pressure condition, which contributes to the fast-strength development in the first 1−2 days after mixing with water.[5]

The hydration route of CA is strongly temperature-dependent; see eq 1:[1−7]

$$CA + H \rightarrow \begin{cases} CAH_{10} & (<10-15°C) \\ C_2AH_8 + AH_3 & (15-30°C) \\ C_3AH_6 + AH_3 & (>30-60°C) \end{cases} \quad (1)$$
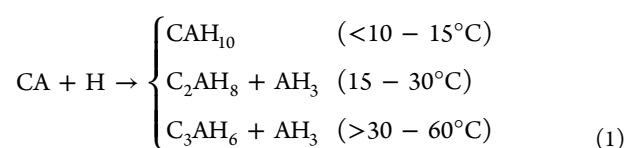
The low-temperature metastable hexagonal phases CAH$_{10}$ and C$_2$AH$_8$ are kinetically stable if the curing temperature remains lower than ~15 °C and ~30 °C, respectively. However, they will inevitably convert to the stable forms, C$_3$AH$_6$ (cubic, with rhombic dodecahedron habit[4]) and AH$_3$ (usually in the form of poorly crystalline gibbsite), over the long-term service life, especially at elevated temperatures. This occurs according to the following reaction equations:[6−8]

$$2CAH_{10} \rightarrow C_2AH_8 + AH_3 + 9H$$

$$3CAH_{10} \rightarrow C_3AH_6 + 2AH_3 + 18H$$

$$3C_2AH_8 \rightarrow 2C_3AH_6 + AH_3 + 9H \quad (2)$$
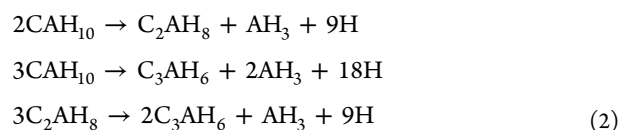
Since the products have higher densities than the initial reactants, this conversion is often accompanied by a marked increase in porosity and a significant loss of strength.[1−5] To compensate for this degradation, the precursor component matrix needs to be very dense before the conversion. This

usually requires the initial water-to-cement mass ratio (w/c) of CAC concrete to be below 0.4.[5] Investigating the mechanism of the conversion reaction has pronounced significance both to the fundamental knowledge of cement chemistry and its engineering applications.

The crystal structures of CAH_{10} and C_3AH_6 are well established;[4,9,10] however, that of C_2AH_8 is still not completely defined, although it is known to be a layer-double-hydroxide (LDH) compound with Al(VI) in the main layer and Al(IV) in the interlayer space.[11,12] The missing information on the C_2AH_8 structure and the unclear relationship between the chemical environments of the metastable and the stable phases add to the difficulty in solving the following fundamental questions regarding the conversion reactions:

(1) At temperatures above ~50 °C, does CAH_{10} convert directly to C_3AH_6[4] or go through an intermediate transformation phase(s), e.g. C_2AH_8?[6]

(2) Does the conversion happen in a through-solution mechanism[15] or by a solid-state reaction?[6]

Previous in situ synchrotron radiation energy-dispersive diffraction (SR-EDD) evidence showed that when CAH_{10} is stored at a constant temperature between 50−90 °C, its conversion to C_3AH_6 undergoes a reaction through an intermediate C_2AH_8, until C_3AH_6 becomes self-nucleated, and that the conversion of CAH_{10} is governed by solid-state reaction mechanisms.[6,13,14] Other research, however, suggests that a through-solution reaction is kinetically favored over a solid-state reaction as the ion transportation inside the solid is extremely slow,[15] and C_2AH_8 precipitates earlier than C_3AH_6 due to the ease of nucleation.[16]

The microstructural evolution of ordinary Portland cement (OPC) hydration has been successfully investigated in the past decades both by experiments and computational modeling.[17,18] To apply such modeling schemes to CAC concrete, the morphological change of converted CAC hydrates at the nano- and micron-scale needs to be clarified. In the meantime, immobilization of toxic (heavy) metals in hardened CAC matrix is gaining increasing interest in environmental engineering practice[19,20] due to its higher resistance to chemical attack and mechanical abrasion compared with OPC. Existing studies suggest that metal ions with different coordination geometries may favor the crystallization of different calcium aluminate hydrates, which would in turn alter the rate of hydration and conversion of CAC cement paste. For example, doping $Zn(NO_3)_2$ leads to the preferential formation of C_2AH_8, whereas CAH_{10} is the prevailing hydrates when $Pb(NO_3)_2$ is doped. Yet this correlation may change as curing temperature increases from 20 to 60 °C.[19] Little evidence exists to describe the mechanism of how metal ions affect the kinetics of hydration and conversion. Understanding the conversion reaction mechanism is critical to further understand and track the chemical status of metallic ions encapsulated within calcium aluminate hydrates, and to assess the reliability of using CAC concrete as a long-term container for metallic ion waste.

The present study uses synchrotron-based scanning transmission X-ray microscopy (STXM)[21] to collect the near-edge X-ray absorption fine structure (NEXAFS) spectra at the Ca $L_{2,3}$-edge and Al K-edge,[22] of the CAH_{10} conversion−reaction system. The spectroscopic information, coupled with ptychographic imaging data at resolutions of ~15 nm,[23] allows direct chemical and morphological observations at the nanometer scale. NEXAFS spectra of the pure phases [CAH_{10}, C_2AH_8,

C_3AH_6, and AH_3 (in gibbsite form)] were first collected, followed by tracking the spatially resolved crystal chemistry evolution of CAH_{10} confined in a water bath at 60 °C. Our results provide nanoscale evidence of how CAH_{10} converts to C_3AH_6 under an elevated temperature, which can be directly used in modeling the microstructural evolution of CAC concrete affected by the conversion reaction.

■ EXPERIMENTAL SECTION

Pure CA and C_3AH_6 were purchased from Mineral Research Processing Cie. Pure CAH_{10} was synthesized by CA hydration in deionized (D.I.) water, according to the protocol established in previous research[8] but using a water-to-CA mass ratio of 10. The hydrates were cured in polypropylene vials for 7 days at 8 ± 2 °C. Crystalline C_2AH_8 with amorphous AH_3 gel was synthesized by CA hydration in deionized water at 25 ± 2 °C and cured in polypropylene vials for 7 days. Both samples were vacuum-filtered in a N_2-protected glovebox. Gibbsite was synthesized by mixing 100 mL of 0.1 M aluminum nitrate hexahydrate aqueous solution with a 0.25% ammonia aqueous solution up to pH 8 at 80 °C. The slurry was then loaded into a flask and heated under constant stirring at 80 °C for 4 days. After being cooled to room temperature, the material was recovered by filtration, washed with deionized water, and dried for 1 day in an oven at 120 °C. These phases were verified by a PANalytical X'Pert Pro^{TR} diffractometer, according to the characteristic x-ray diffraction (XRD) peak positions of each phase.[4,8] The pure CAH_{10}, C_3AH_6, and gibbsite samples were used to collect reference spectra at the Ca $L_{2,3}$-edge and Al K-edge. The hexagonal-shaped C_2AH_8 single crystals are readily identified from amorphous AH_3 under STXM and are used to collect the reference spectra for C_2AH_8.

The aforementioned CAH_{10}−D.I. water suspension, contained in 2 mL polypropylene vials, was rapidly heated to 60 ± 2 °C in a water bath. After being heated for the desired time durations (30 min, 1 h, and 3 h), a 0.1 µL drop of the suspension was transferred onto a 100 nm-thick-Si_3N_4 window, followed by quick removal of the liquid with Kimwipes (Kimtech Science^{TR}), as described in ref 22. The top of the sample was covered with another Si_3N_4 window. Epoxy-glue was applied along the perimeter edges of the two windows in order to isolate the solid samples from the relative humidity of the experimental environment. The "sandwiched" sample was then placed in the STXM chamber for measurements.

The STXM experiments at Ca $L_{2,3}$-edge were conducted at beamline 5.3.2.2, and Al K-edge at beamline 5.3.2.1, of the Advanced Light Source of the Lawrence Berkeley National Laboratory. This synchrotron radiation facility operates at 1.9 GeV and 500 mA. Beamline 5.3.2.2 provides X-ray beam energy in the range of 250−780 eV,[24] using a zone plate with the smallest zone width of 25 nm that yields transmission images at a resolution of ~30 nm. Beamline 5.3.2.1 covers the X-ray beam energy range from 600 to 2000 eV. It is coupled with a fast CCD for ptychographic imaging at a pixel resolution ~5 nm, using soft X-ray beam at energy 800 eV.[23] The effective resolution for this study was ~15 nm. For the current study, the energy scanning range is 340−360 eV (step size 0.1 eV) for the Ca $L_{2,3}$-edge, and 1550−1610 eV (step size 0.2 eV) for the Al K-edge. The measured data were processed using aXis2000 software, and the spectra were normalized for comparison purposes.[22] A single-value-decomposition (SVD) algorithm is imbedded in aXis2000, which allows fitting a target spectrum using linear combination of several reference spectra.

■ RESULTS AND DISCUSSION

Ca $L_{2,3}$-Edge NEXAFS Spectroscopic Study of CAH_{10}, C_2AH_8, and C_3AH_6. The Ca $L_{2,3}$-edge NEXAFS spectra contain the coordination environment information on the Ca−O polyhedra in the pure phases. The interpretation here follows the theory of crystal field splitting of d^0 compounds such as Ca^{2+}, which is briefly described in previous research of Ca-bearing minerals in cement-related systems;[22,25] detailed
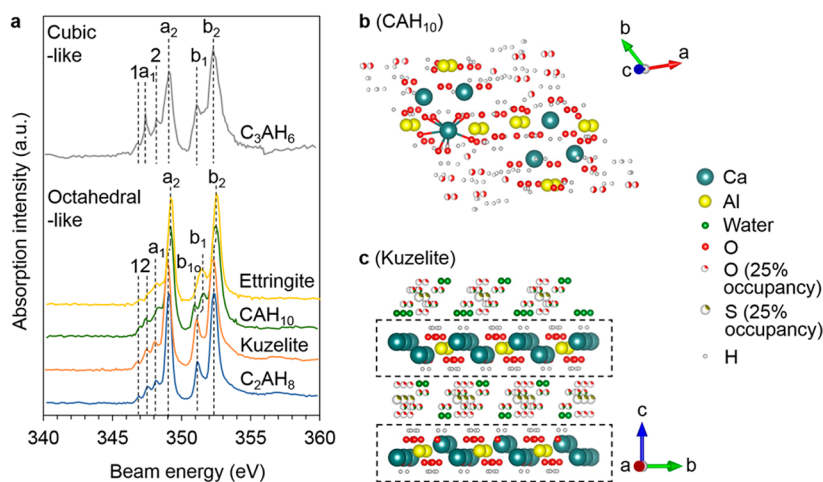
Figure 1. (a) Ca $L_{2,3}$-edge NEXAFS spectra of CAH_{10}, C_2AH_8, and C_3AH_6, with the spectra of ettringite and kuzelite displayed as references;[22] (b) atomic configuration of CAH_{10}[28] where the bonds in one CaO_8 complex are displayed; and (c) atomic configuration of kuzelite[30] (monosulfate-AFm) where the layer structure $[Ca_2Al(OH)_6]^+$ is illustrated by dashed squares.
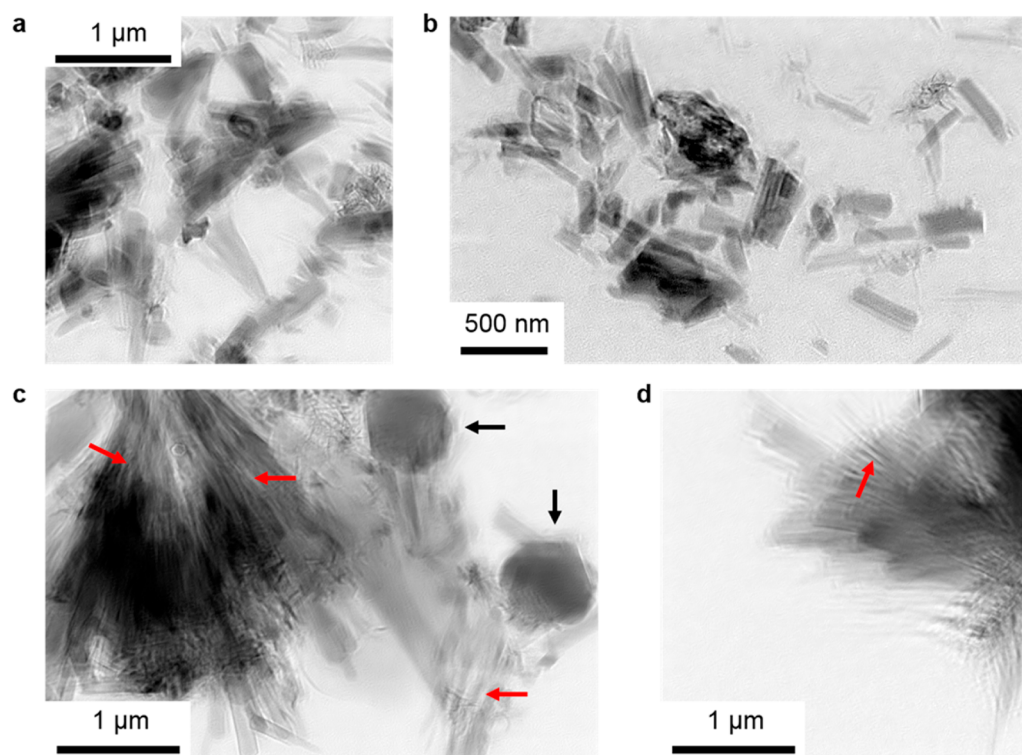

Figure 2. X-ray ptychographic images of CAH_{10} crystals: (a) and (b) before being subjected to heat curing; (c) and (d) after being stored at 60 ± 2 °C for 30 min. The black arrows indicate the C_3AH_6 crystals, and the red arrows point to the clear morphological change in CAH_{10} prisms.

theoretical background can be found in the literature.[26,27] In summary, a typical Ca $L_{2,3}$-edge NEXAFS spectrum has two doublets due to spin−orbital coupling. Each doublet has a major (a_2 or b_2) and a minor peak (a_1 or b_1); see Figure 1a. A few leading peaks (named peak 1 and 2 herein) may also be present before the first doublet. For d^0 compounds, the d orbitals are classified into t_{2g} symmetry (d_{xy}, d_{yz}, and d_{xz}) and e_g symmetry (d_{z^2} and $d_{x^2-y^2}$). They have equal energy until they are approached by ligands (O atoms in this study), which change the energy of the d orbitals depending on the coordination symmetry. As a result, the energy gap e_g-t_{2g}, also termed $10Dq$, is sensitive to the symmetry of the complexation. The characteristics of the spectra, i.e., the distance and relative

intensity between the major and minor peaks, are greatly influenced by $10Dq$ and the coordination symmetry; therefore, they can be used as an index of the chemical environment of Ca.[22,25]

The Ca−O coordination of C_3AH_6 is cubic-like as the peak 2 of the Ca $L_{2,3}$-edge NEXAFS spectrum is located between peak a_1 and a_2; see Figure 1a.[22] In contrast, the coordination of Ca−O in CAH_{10} and C_2AH_8 are octahedral-like, similar in shape to ettringite and kuzelite (also named monosulfate-AFm). As shown in Figure 1b, the atomic configuration of Ca−O polyhedron in CAH_{10}[28] is very similar to that of ettringite:[22,29] a rectangle (four O atoms) and a parallelogram (four O atoms) approach the Ca from opposite directions and are aligned along
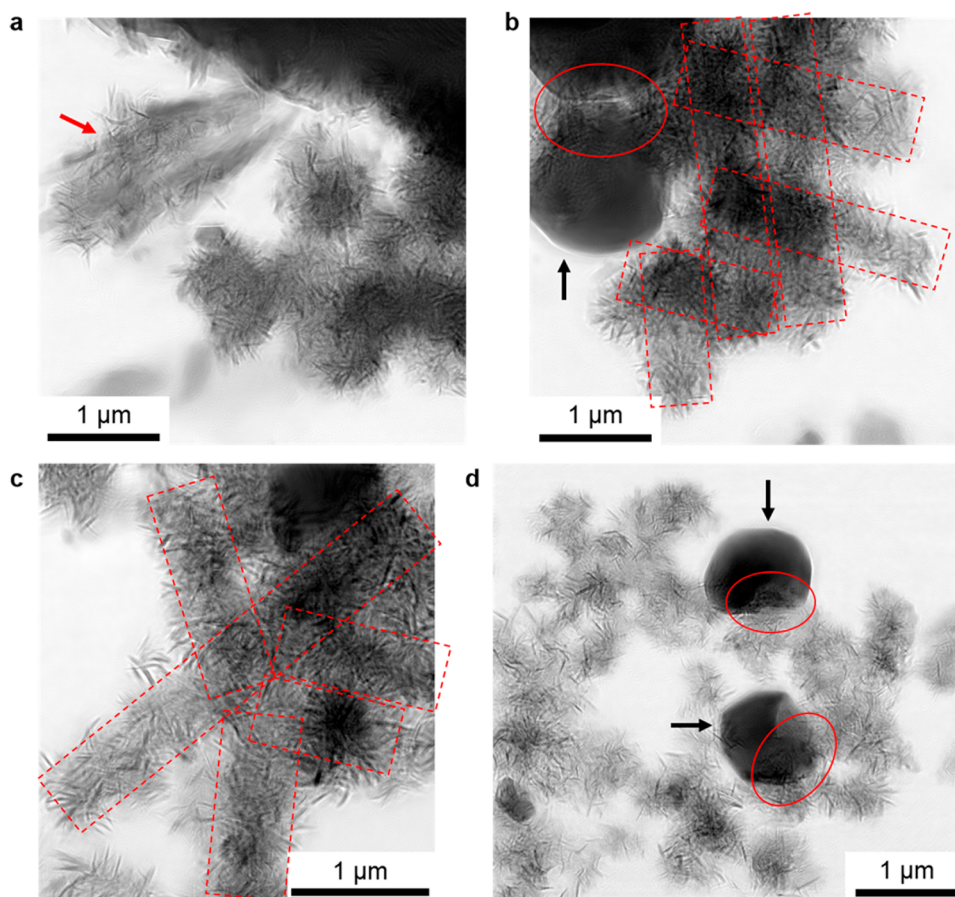
Figure 3. (a−d) X-ray ptychographic images of CAH_{10} stored at 60 ± 2 °C for 60 min. The black and red arrows indicate the C_3AH_6 particles and a CAH_{10} prisms cluster in the middle of conversion, respectively. The red circles indicate the close contact between C_3AH_6 crystals and the fiber morphology. The red dashed boxes indicate the prismatic contour of the fiber morphology.

each other's diagonals. The main peak (a_2 or b_2) positions of their Ca $L_{2,3}$-edge spectra are both ∼0.2 eV higher than those of kuzelite and C_2AH_8; see Figure 1a. The spectra of CAH_{10} also has a clearly resolved b_{1o} peak between peak a_2 and b_1, which is not observed in ettringite, and can be used to distinguish these two phases in a Ca K-edge STXM study.

The atom positions of the C_2AH_8 have not been determined yet.[11] The results presented herein strongly imply the existence of a $[Ca_2Al(OH)_6]^+$ layer structure in C_2AH_8, which is highly similar to kuzelite, because they share almost identical Ca $L_{2,3}$-edge spectra. In contrast, the interlayer $[SO_4]^-$ anion groups in kuzelite are replaced by $[AlO_4]^{3-}$ groups in C_2AH_8; see Figure 1c.[11] Therefore, in both minerals, Ca is in a 3-fold rotation site, coordinated by seven oxygen neighbors. This slightly lowers the oxidation degree of Ca compared to those in CAH_{10}, ettringite, and C_3AH_6 where the Ca–O coordination number is 8. Therefore, the main peak (a_2 or b_2) positions in C_2AH_8 and kuzelite are ∼0.2 eV lower.

X-ray Ptychographic Image and Al K-Edge NEXAFS Study of the Conversion Reaction. Before Heat Curing and after 30 min Storage in a 60 °C Water Bath. Compared to a transmission electron microscope, X-ray ptychographic imaging provides nanometer resolution but with much less beam damage to the samples. As shown in Figure 2a,b, prismatic CAH_{10} crystals are synthesized from CA hydration at 8 °C. The crystals in the field of view are of similar size, with length 0.5–1 μm and width 150–500 nm. Particles can agglomerate up to ∼1 μm wide; see Figure 2a,b. After 30 min

storage in a 60 ± 2 °C water bath, clear morphological changes occur to the prismatic CAH_{10} as parallel gaps form along the longitudinal direction (red arrows in Figure 2c,d). Faceted particles with diameters of ∼700 nm are observed (black arrows in Figure 1c). On the basis of the round morphology, they are identified as C_3AH_6, which has the characteristic rhombic dodecahedron habit of cubic garnets.[4,15] This will be confirmed in the next section by spectroscopic evidence.

After 60 min storage in a 60 °C water bath, the CAH_{10} prisms are no longer widely observed; see Figure 3. Instead, the main morphology is the agglomerations of thin short fibers, which are of similar size, i.e., 100–200 nm long and a few tens of nanometers thick. The contour of the fiber agglomerations is highly similar to the original CAH_{10} prisms, as illustrated by the red dashed squares in Figure 3b,c. An aggregated CAH_{10} prism cluster is observed in the middle of conversion to thin short fibers (red arrow in Figure 3a). The prisms have not completely disappeared, while fiber networks seem to be forming in a random orientation inside the region which was originally occupied by CAH_{10} prisms. The fibers are less likely to nucleate on the CAH_{10} surface in which case a specific orientation of fibers on the surface should be expected. Faceted C_3AH_6 particles (black arrow in Figure 3b,d), with diameter ∼1 μm, are also observed to be in close contact with the fiber networks on 1−2 facets; see red circles in Figure 3b,d.

The previous description of morphological changes seems to indicate a solid-state transformation from CAH_{10} to the agglomerations of fibers of much smaller size relative to
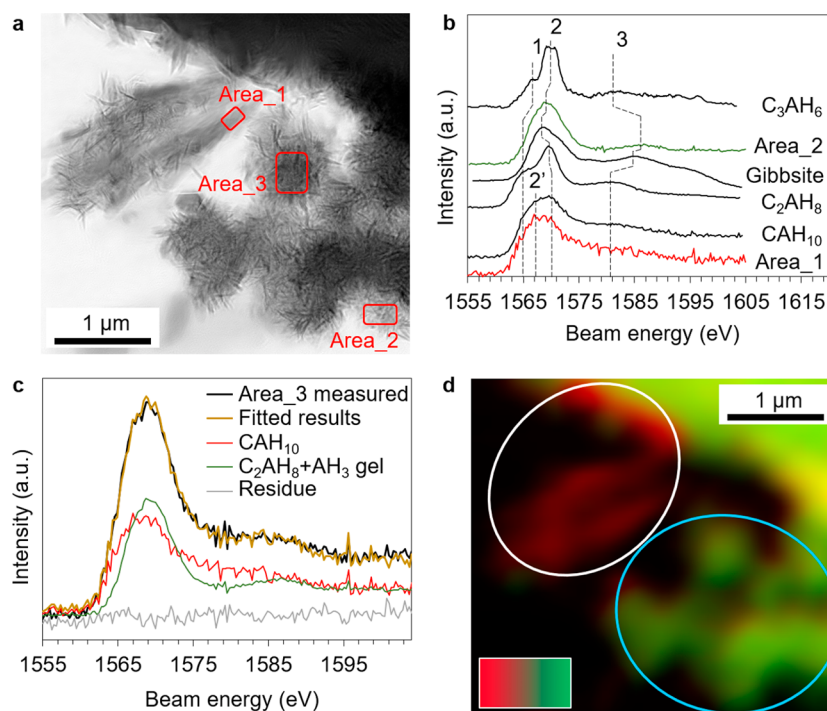
Figure 4. Al K-edge NEXAFS study of CAH_{10} stored at 60 ± 2 °C for 60 min: (a) ptychographic image of the studied region, with areas of interests indicated by red squares; (b) Al K-edge spectra of pure phases (black curves) and areas of distinct morphology in (a) (Area_1 in red and Area_2 in green); (c) the measured and SVD fitted spectra of Area_3, using the spectra of CAH_{10} and $C_2AH_8 + AH_3$ as single components; and (d) the phase distribution of the studied area is mapped out by assigning red and green to CAH_{10} and $C_2AH_8 + AH_3$ gel, respectively. The inset demonstrates the red-green color mixing for reading convenience.

CAH_{10} prisms. To confirm this observation, a spatially resolved Al K-edge NEXAFS study was conducted in the area of Figure 3a, as shown in Figure 4. The reference spectra of pure phases (Figure 4b) are consistent with the reported work apart from the different energy calibration standards used.[31,32] In general, the major absorption of the pure phases are composed of a few individual peaks, which correspond to the major $1s$ to $3p$ transition (peak 1) and the multiple scattering (MS) process from the neighboring shells (peak 2).[32,33] The ratio between the intensities of the $1s \rightarrow 3p$ transition and the MS process can vary significantly. For example, in the spectra of gibbsite, C_2AH_8, and C_3AH_6, the MS peak is dominant, whereas in CAH_{10}, it has comparable intensity to the $1s \rightarrow 3p$ transition peak. A minor peak 3 is usually observed at ~15 eV higher than the major peaks, which can be attributed to either the MS process or a transition from 1s to 3d. Although theoretical prediction of the spectra is complex, the abundant spectral characteristics allow reliable component phase mapping.[34]

To investigate the chemical information on areas with distinct morphologies, the Al K-edge NEXAFS spectra of Area_1 and Area_2 are investigated (Figure 4a,b) since they each represent a morphological type, i.e., the prisms (Area_1) and fiber agglomeration (Area_2). The spectrum of Area_1 highly resembles that of pure CAH_{10} in both peak positions and relative intensities. Area_1 is therefore assigned to a CAH_{10} prism that has not yet converted to the final product. Among all reference spectra, the spectrum of Area_2 resembles that of AH_3 (gibbsite) most closely. The peak 3 of both Area_2 and gibbsite is at a much higher position than that of other reference phases. However, the major peak position of Area_2 is ~0.8 eV higher compared to that of gibbsite, which can be explained by the contribution from C_2AH_8 and/or C_3AH_6. The

spectrum of Area_2 clearly does not match that of CAH_{10} in either the position or the broadness of the major peak (peak 2) as well as the position of the minor peak (peak 3). Further evidence is given in the Supporting Information (SI), where single value decompositions (SVD) of the major peak of Area_2 spectrum, using the above-mentioned reference spectra, leads to a negative and insignificant coefficient for CAH_{10} spectrum, which is obviously unrealistic. The Area_2 spectrum can be satisfactorily fit using AH_3 combined with either C_2AH_8 or C_3AH_6; see SI file for details.

It is reported that C_2AH_8 crystallizes in the beginning of CAH_{10} conversion reaction.[6] Considering the shape of the short fibers, they are more likely C_2AH_8 (hexagonal crystal shape), rather than C_3AH_6 (cubic crystal shape). Reported research has also confirmed that the AH_3, formed from the conversion of CAH_{10}, often exists as an amorphous gel that cannot be detected by XRD.[6,8,13,14] Therefore, Area_2 is most probably composed of aggregated short fibers of C_2AH_8 intermixed with AH_3 gel. The coexistence of C_2AH_8 and AH_3 gel is consistent with the reaction formula; see eq 2.

We then investigated a much thicker region; see Area_3 in Figure 4a. As shown in Figure 4c, the spectrum of Area_3 can be well fitted by the linear combination of the reference spectra of Area_1 (CAH_{10}) and Area_2 ($C_2AH_8 + AH_3$ gel), which confirms that Area_3 contains residual CAH_{10} and the conversion products, i.e., $C_2AH_8 + AH_3$ gel. From a quantitative analysis point of view, the prepeak and postpeak baseline intensities of two reference spectra components in Figure 4c, i.e., CAH_{10} (red curve) and $C_2AH_8 + AH_3$ gel (green curve), are almost identical. Previous literature demonstrates that the difference between the prepeak and postpeak baseline intensity is linearly proportional to the amount of attenuation created
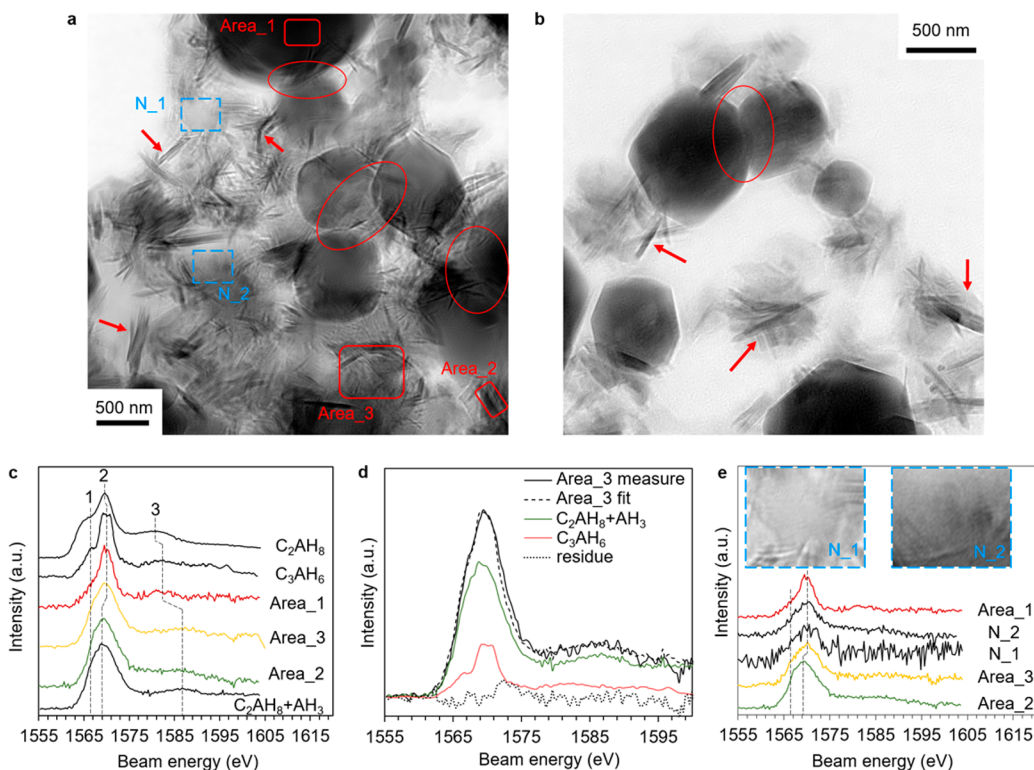
Figure 5. Al K-edge NEXAFS and X-ray ptychographic images studies of CAH_{10} stored in a 60 ± 2 °C water bath for 180 min: (a) and (b) Ptychographic images of converted CAH_{10} where the red circles indicate the close contact between C_3AH_6 dodecahedra, and the red arrows point to the fibrillar features; (c) and (e) Al K-edge NEXAFS spectra of selected regions in (a), compared with spectra of pure phases. The insets in (e) are enlarged images of Area N_1 and N_2 in (a). (d) The measured and SVD fitted spectra of Area_3 in (a), using the spectra of C_3AH_6 + AH_3 and CAH_{10} as single components.

due to the absorption edge of Al.[22] Therefore, in Area_3, the amount of Al from CAH_{10} and C_2AH_8 + AH_3 gel is roughly the same. It should be noted that Area_2 may also contain residue CAH_{10}; however, we chose this visually thin area with uniquely distinguished morphology (agglomerated fibers) so that the chance of CAH_{10} be mixed in Area_2 is significantly low.

By applying the same fitting strategy to the whole studied region, a phase mapping is displayed in Figure 4d with red representing CAH_{10} and green representing C_2AH_8 + AH_3 gel. The prismatic morphology is mainly assigned to CAH_{10} (white circles in Figure 4d), and the region of short fibers (blue circles in Figure 4d) is mainly assigned to C_2AH_8 + AH_3, with contributions of CAH_{10} spectrum in the thick areas. Coupled with the morphological observation that the short fibers agglomerate in the contour of the original CAH_{10} prism, the spectroscopic evidence leads to the hypothesis that CAH_{10} converts to C_2AH_8 fibers and AH_3 gel through internal decomposition, i.e., C_2AH_8 + AH_3 gel form within the region which was originally occupied by CAH_{10} prisms. In such case, the conversion reaction happens in a solid-state route, and the external bulk water is not needed to transport dissolved ions.

Although C_2AH_8 has been detected by XRD as an intermediate phase before CAH_{10} converts to C_3AH_6,[13,14] long-standing doubts exist as to whether a direct solid-state transformation from CAH_{10} to C_2AH_8 occurs because it is not kinetically favored; i.e., the ion diffusion within the solid phase is much slower than in the aqueous environment under the current temperature.[15] However, as verified in Figure 3, C_2AH_8 forms in the shape of numerous thin fibers instead of a few big crystals. The size of each fiber and the distance between

adjacent fibers are within a few tens of nanometers. Considering a simplified diffusion case from a thin-plate source into a semi-infinite solid, the concentration of the diffused phase is inversely proportional to the exponent of the square of the distance from the thin-plate source.[35] Therefore, compared with the case of 500 nm diffusion distance, the time needed for ions exchange from the fiber region into the adjacent nonfiber region is several tens of orders of magnitude less. This would largely lower the kinetic difficulty of ion diffusion in the solid-state reaction. At 60 °C, this nanoscale ion transportation is rapid enough to decompose a large crystal of CAH_{10} to crystalline Ca-rich regions (C_2AH_8) and amorphous Al-rich regions (AH_3 gel) within an hour of incubation.

After 180 min storage in a 60 °C water bath, with storage at 60 ± 2 °C for 180 min, we observe an enrichment of the faceted C_3AH_6 dodecahedral crystals (Figure 5); however, their sizes are not significantly larger, compared with water bath for 30 and 60 min. The proximity of adjacent C_3AH_6 dodecahedra facets indicates that C_3AH_6 may crystallize on the facets of existing C_3AH_6 crystals, as indicated by the red circles in Figure 5a,b. After 180 min of thermal storage, the fibrillar morphology of C_2AH_8 (previously observed after 60 min of thermal storage) are still present but seem to decrease in number but increase in thickness (red arrows in Figure 5a,b). Apart from these crystalline morphologies, areas exist that lack crystalline features; see Area_3, N_1, and N_2 in Figure 5a.

To investigate the chemistry of areas with distinct morphologies, Al K-edge NEXAFS spectra of Area_1 (round crystal), Area_2 (fibrillar crystal), and Area_3 (fibers intermixed with featureless phase) were collected; see Figure

5c. It is easily confirmed by comparing the spectra Area_1 and C_3AH_6 that the particles are C_3AH_6. The spectrum of fibrillar phases (Area_2) resembles the spectrum of the fibrillar area in Figure 4a, which is confirmed to be a mixture of C_2AH_8 and AH_3 gel. The major peak position (peak 2) in the spectrum of Area_3 (Figure 5c) matches that of C_3AH_6, yet the former is much broader. This broadness can be explained by the contributions from remnant $C_2AH_8 + AH_3$ that exhibits the fibrillar feature. As shown in Figure 5d, the spectrum of Area_3 can be well-fitted using a linear combination of the spectra of $(C_2AH_8 + AH_3)$ and C_3AH_6 at a mass ratio of ~2.5. We investigate two other poorly crystalline areas, N_1 and N_2, which exhibit featureless morphologies that were similar to Area_3, with residue of fibrillar features; see the enlarged images of N_1 and N_2 in Figure 5e. The spectra of N_1 and N_2 also resemble that of Area_3 in Figure 5c; i.e., there is clear contribution from C_3AH_6 spectrum to their major peak positions and contribution from $C_2AH_8 + AH_3$ to the major peak broadness. Therefore, the featureless areas in Area_3, N_1 and N_2 are most likely poorly crystalline C_3AH_6 precursors, intermixed with remnant crystalline region of C_2AH_8. This is consistent with previous findings that C_2AH_8 provides a nucleation site for C_3AH_6.[6]

The C_3AH_6 crystallized to individual particles with a unique dodecahedral shape, which are distinct to the prismatic or fibrillar shapes of the metastable phases. This initial crystallization implies a through-solution, rather than a solid-state reaction path. As shown in Figures 2, 3, and 5, the existing C_2AH_8 and C_3AH_6 crystals seem to act as preferred nucleation sites for C_3AH_6. Therefore, the formation of C_3AH_6 may be self-accelerated when nucleation is factored into the rate-control process.[14] It should also be noticed that C_2AH_8 does not grow to macrocrystals throughout the heating duration in this study, and the number of C_2AH_8 crystals soon decreases after ~1 h of thermal storage. This explains why the maximum diffraction signal of C_2AH_8 remains low compared with that of CAH_{10}, as shown by the SR-EDD study.[6] In real CAC concrete infrastructure, the rate of conversion may differ from the current study due to the difference of reaction conditions. Therefore, the percentage and morphology of CAH_{10}, C_2AH_8, and C_3AH_6 in a converted infrastructure are functions of the local temperature, local ion concentration, and spatial availability for crystal growth.

CONCLUSION

The current study used nanometer resolved Ca $L_{2,3}$-edge and Al K-edge NEXAFS spectroscopy to investigate the conversion reaction of CAH_{10} at an elevated temperature (60 °C). Our results provide solid evidence that solves the decades-long debate regarding conversion reaction mechanisms. The results are summarized as follows:

(1) Although the atomic positions of C_2AH_8 are not completely solved, we provide spectroscopic evidence to prove that the local environment of Ca in the layer structure $([Ca_2Al(OH)_6]^+)$ of C_2AH_8 highly resembles that of kuzelite. The Ca K-edge spectra reported here can be used as reference spectra for future study at Ca K-edge.

(2) After storage in a 60 °C water bath for 60 min, the prismatic CAH_{10} decomposed to thin fibers of C_2AH_8 and amorphous AH_3 in a solid-state route through short-range ion transportation within a few tens of nanometers.

(3) Upon extended incubation for 180 min under 60 °C, the C_2AH_8 destabilized to form C_3AH_6 in a through-solution route. Existing C_2AH_8 and C_3AH_6 crystals may act as preferred nucleation sites for C_3AH_6 crystallization.

Understanding the mechanism of the conversion reaction in CAC is fundamentally important to innovate and implement control strategies at the reaction stage. Future work may include quantitatively correlating the solid-state decomposition rate of CAH_{10} with the external conditions, such as the relative humidity and curing temperature. In the application of immobilizing heavy metals, the internal condition of CAH_{10}, such as the changing coordination geometries of the incorporated metallic ions, may alter the kinetics and path of the conversion reaction. This study presents a coupled morphological and spectroscopic tool to reveal such process at the nanoscale.

ASSOCIATED CONTENT

Ⓢ Supporting Information

The Supporting Information is available free of charge on the ACS Publications website at DOI: 10.1021/acs.cgd.7b00553.

A single value decomposition (SVD) of the Area_2 spectrum in Figure 4 (PDF)

AUTHOR INFORMATION

Corresponding Author
*E-mail: monteiro@berkeley.edu.
ORCID Ⓞ
Paulo J. M. Monteiro: 0000-0002-6866-1783

Notes
The authors declare no competing financial interest.

ACKNOWLEDGMENTS

REFERENCES

(1) Mehta, P. K.; Monteiro, P. J. M. *Concrete Microstructure, Properties, and Materials*, 4th ed.; McGraw-Hill Companies: New York City, 2014.
(2) Barnes, P.; Bensted, J. *Structure and Performance of Cements*; CRC Press: Boca Raton, 2002.
(3) Taylor, H. F. *Cement Chemistry*, 2nd ed.; Thomas Telford: London, 1997.
(4) Pöllmann, H. Calcium Aluminate Cements—Raw Materials, Differences, Hydration and Properties. *Rev. Mineral. Geochem.* **2012**, *74*, 1−82.
(5) Scrivener, K. L.; Cabiron, J. L.; Letourneux, R. High-performance Concretes from Calcium Aluminate Cements. *Cem. Concr. Res.* **1999**, *29*, 1215−1223.
(6) Rashid, S.; Barnes, P.; Bensted, J.; Turrillas, X. Conversion of Calcium Aluminate Cement Hydrates Re-examined with Synchrotron Energy-Dispersive Diffraction. *J. Mater. Sci. Lett.* **1994**, *13*, 1232−1234.
(7) Edmonds, R. N.; Majumdar, A. J. The Hydration of Monocalcium Aluminate at Different Temperatures. *Cem. Concr. Res.* **1988**, *18*, 311−20.
(8) Jensen, T. R.; Christensen, A. N.; Hanson, J. C. Hydrothermal Transformation of the Calcium Aluminum Oxide Hydrates $CaAl_2O_4$·

10H$_2$O and Ca$_2$Al$_2$O$_5$·8H$_2$O to Ca$_3$Al$_2$(OH)$_{12}$ Investigated by in situ Synchrotron X-ray Powder Diffraction. *Cem. Concr. Res.* **2005**, *35*, 2300−2309.

(9) Christensen, A. N.; Lebech, B.; Sheptyakov, D.; Hanson, J. C. Structure of Calcium Aluminate Decahydrate (CaAl$_2$O$_4$·10D$_2$O) from Neutron and X-ray Powder Diffraction Data. *Acta Crystallogr., Sect. B: Struct. Sci.* **2007**, *63*, 850−861.

(10) Lager, G. A.; Armbruster, T.; Faber, J. Neutron and X-ray Diffraction Study of Hydrogarnet Ca$_3$Al$_2$(O$_4$H$_4$)$_3$. *Am. Mineral.* **1987**, *72* (7−8), 756−765.

(11) Ukrainczyk, N.; Matusinovic, T.; Kurajica, S.; Zimmermann, B.; Sipusic, J. Dehydration of a Layered Double Hydroxide—C$_2$AH$_8$. *Thermochim. Acta* **2007**, *464*, 7−15.

(12) Richard, N.; Lequeux, N.; Boch, P. EXAFS Study of Refractory Cement Phases: CaAl$_2$O$_{14}$H$_{20}$, Ca$_2$Al$_2$O$_{13}$H$_{16}$, and Ca$_3$Al$_2$O$_{12}$H$_{12}$. *J. Phys. III.* **1995**, *5*, 1849−1864.

(13) Rashid, S.; Barnes, P.; Turrillas, X. The Rapid Conversion of Calcium Aluminate Cement Hydrates, as Revealed by Synchrotron Energy-Dispersive Diffraction. *Adv. Cem. Res.* **1992**, *4*, 61−67.

(14) Rashid, S.; Turrillas, X. Hydration Kinetics of CaAl$_2$O$_4$ Using Synchrotron Energy-Dispersive Diffraction. *Thermochim. Acta* **1997**, *302*, 25−34.

(15) Bradbury, C.; Callaway, P. M.; Double, D. D. The Conversion of High Alumina Cement/Concrete. *Mater. Sci. Eng.* **1976**, *23*, 43−53.

(16) Newman, J.; Choo, B. S. *Advanced Concrete Technology: Constituent Materials*; John Wiley & Sons: New York City, 2003.

(17) Bentz, D. P. Three-Dimensional Computer Simulation of Portland Cement Hydration and Microstructure Development. *J. Am. Ceram. Soc.* **1997**, *80*, 3−21.

(18) Thomas, J. J.; Biernacki, J. J.; Bullard, J. W.; Bishnoi, S.; Dolado, J. S.; Scherer, G. W.; Luttge, A. Modeling and Simulation of Cement Hydration Kinetics and Microstructure Development. *Cem. Concr. Res.* **2011**, *41*, 1257−1278.

(19) Navarro-Blasco, I.; Duran, A.; Sirera, R.; Fernandez, J. M.; Alvarez, J. I. Solidification/Stabilization of Toxic Metals in Calcium Aluminate Cement Matrices. *J. Hazard. Mater.* **2013**, *260*, 89−103.

(20) Ukrainczyk, N.; Vrbos, N.; Šipušić, J. Influence of Metal Chloride Salts on Calcium Aluminate Cement Hydration. *Adv. Cem. Res.* **2012**, *24*, 249−262.

(21) Geng, G.; Taylor, R.; Bae, S.; Hernández-Cruz, D.; Kilcoyne, D. A.; Emwas, A. H.; Monteiro, P. J. Atomic and Nano-Scale Characterization of a 50-Year-Old Hydrated C$_3$S Paste. *Cem. Concr. Res.* **2015**, *77*, 36−46.

(22) Geng, G.; Myers, R. J.; Kilcoyne, A. L. D.; Ha, J.; Monteiro, P. J. M. Ca L$_{2,3}$-edge Near Edge X-ray Absorption Fine Structure of Tricalcium Aluminate, Gypsum and Calcium (Sulfo)Aluminate Hydrates. *Am. Mineral.* **2017**, *102*, 900.

(23) Shapiro, D. A.; Yu, Y. S.; Tyliszczak, T.; Cabana, J.; Celestre, R.; Chao, W.; Kaznatcheev, K.; Kilcoyne, A. D.; Maia, F.; Marchesini, S.; Meng, Y. S.; et al. Chemical Composition Mapping with Nanometre Resolution by Soft X-ray Microscopy. *Nat. Photonics* **2014**, *8*, 765−769.

(24) Kilcoyne, A. L. D.; Tyliszczak, T.; Steele, W. F.; Fakra, S.; Hitchcock, P.; Franck, K.; Anderson, E.; Harteneck, B.; Rightor, E. G.; Mitchell, G. E.; Hitchcock, A. P.; et al. Interferometer-controlled scanning transmission X-ray microscopes at the Advanced Light Source. *J. Synchrotron Radiat.* **2003**, *10*, 125−136.

(25) Fleet, M. E.; Liu, X. Calcium L$_{2,3}$-edge XANES of Carbonates, Carbonate Apatite, and Oldhamite (CaS). *Am. Mineral.* **2009**, *94*, 1235−1241.

(26) De Groot, F. M. F.; Fuggle, J. C.; Thole, B. T.; Sawatzky, G. A. L$_{2,3}$ X-ray-Absorption Edges of d^0 Compounds: K$^+$, Ca^{2+}, Sc^{3+}, and Ti^{4+} in O$_h$ (Octahedral) Symmetry. *Phys. Rev. B: Condens. Matter Mater. Phys.* **1990**, *41*, 928.

(27) Albright, T. A.; Burdett, J. K.; Whangbo, M. H. *Orbital Interactions in Chemistry*; John Wiley & Sons: New York City, 2013.

(28) Christensen, A. N.; Lebech, B.; Sheptyakov, D.; Hanson, J. C. Structure of Calcium Aluminate Decahydrate (CaAl$_2$O$_4$·10D$_2$O) from Neutron and X-ray Powder Diffraction Data. *Acta Crystallogr., Sect. B: Struct. Sci.* **2007**, *63*, 850−861.

(29) Moore, A. E.; Taylor, H. F. W. Crystal structure of ettringite. *Acta Crystallogr., Sect. B: Struct. Crystallogr. Cryst. Chem.* **1970**, *26*, 386−393.

(30) Allmann, R. Refinement of the Hybrid Layer Structure [Ca$_2$Al(OH)$_6$]$^+$·[1/2SO$_4$·3H$_2$O]$^-$. *Neues. Jb. Miner. Moant.* **1977**, 136−143.

(31) Richard, N.; Lequeux, N.; Boch, P. An X-ray Absorption Study of Phases Formed in High-Alumina Cements. *Adv. Cem. Res.* **1995**, *7*, 159−169.

(32) Ildefonse, P.; Cabaret, D.; Sainctavit, P.; Calas, G.; Flank, A. M.; Lagarde, P. Aluminium X-ray Absorption Near Edge Structure in Model Compounds and Earth's Surface Minerals. *Phys. Chem. Miner.* **1998**, *25*, 112−121.

(33) Li, D.; Bancroft, G. M.; Fleet, M. E.; Feng, X. H.; Pan, Y. Al K-edge XANES Spectra of Aluminosilicate Minerals. *Am. Mineral.* **1995**, *80*, 432−440.

(34) Wieland, E.; Dähn, R.; Vespa, M.; Lothenbach, B. Micro-Spectroscopic Investigation of Al and S Speciation in Hardened Cement Paste. *Cem. Concr. Res.* **2010**, *40*, 885−891.

(35) Borg, R. J.; Dienes, G. J. *An Introduction to Solid State Diffusion*; Elsevier: Amsterdam, 2012.